Original Paper

Deep-detection of formation boundary using transient multicomponent electromagnetic logging measurements

Xi-Yong Yuan [a, b], Shao-Gui Deng [a, *], Zhi-Qiang Li [c], Xiao-Mei Han [b], Xu-Fei Hu [d]

[a] Key Laboratory of Deep Oil and Gas, China University of Petroleum (East China), Qingdao, Shandong, 266580, China
[b] Sinopec Matrix Corporation, Qingdao, Shandong, 266000, China
[c] China Research Institute of Radiowave Propagation, Xinxiang, Henan, 453000, China
[d] China University of Petroleum—Beijing at Karamay, Karamay, Xinjiang, 834000, China

A B S T R A C T

The maximum distance at which an electromagnetic (EM) logging while drilling (LWD) tool detects an approaching boundary is defined as the depth of detection (DOD). Ultra-deep detection capability of the transient multicomponent EM logging measurement is investigated here. First, we adopt sine and cosine transform to calculate the transient multicomponent responses. Compared to the cosine transform, sine transform is more accurate in solving late-time responses. Then, a time-domain geosignal is introduced to sense the boundary. Results show that DOD of this transient EM measurement can be up to tens of meters, including directionally sensitivity. Additionally, by studying the decay characteristics of different components with time, cross component is confirmed to decay much faster than the coaxial/coplanar components in the formation coordinate system. A pseudo-inversion is thereby proposed to determine the dip angle of anisotropic stratified formation. Theoretical simulation results indicate that this algebraic method can determine the true dip at some particular moments. It is still stable and valid even when considering random measurement errors. Moreover, we establish the linear relationship between the time at which the half-point of geosignal curve appears and the distance to boundary (DTB), which would assist in the quick determination of DTB.

© 2021 The Authors. Publishing services by Elsevier B.V. on behalf of KeAi Communications Co. Ltd. This is an open access article under the CC BY-NC-ND license (http://creativecommons.org/licenses/by-nc-nd/4.0/).

1. Introduction

Geosteering measurements, which is crucial to the exploration and production in high-angle and horizontal wells, have long been interested by drilling services and oil companies. The maximum distance at which an electromagnetic (EM) logging while drilling (LWD) tool can sense a formation boundary is defined as the depth of detection (DOD), which is the key to its geosteering ability (Li and Zhou, 2017). With the successful introduction of frequency-domain EM LWD tools that use transverse and tilted antennas, directional geosteering with boundary positions become possible (Li et al., 2005; Shao et al., 2013; Hong et al., 2014; Li and Wang, 2016). DOD of these measurements is typically in the 3—4 m range. To further improve the DOD, oil service companies have developed frequency-domain ultra-deep directional resistivity (DDR) tools to

extend the DOD to 30 m or more away from the wellbore, answered the need for strategic geosteering (Seydoux et al., 2014; Li et al., 2018; Wang et al., 2019a,b; Wu et al., 2020). However, excessive length of these tools would cause inconveniences in applications.

Transient electromagnetic (TEM) method measures the decaying secondary field caused by the abrupt termination of a constant current and possess a deep-reading capability. It has been extensively used in subsurface geological surveys including ground-penetrating radar, deep crustal sounding, groundwater exploration, mining exploration and monitoring etc (Sun et al., 2013; Li et al., 2016). Many geophysicists have also investigated the potential of TEM in well logging these years. Anderson and Chew (1989) use an inverse FFT to calculate the transient induction logging responses. To predict the formation ahead of drill bit, Zhou (2000) proposes a time-domain method to extract the secondary field,

which is subtracted the directed field from the total field. Dutta (2012) proposes a new transient borehole system for reservoir monitoring, defined an incremental signal similar to the secondary field, and proved the effectiveness in evaluating waterflooded reservoir models. Swidinsky and Weiss (2017) firstly use a coincident loop transient induction wireline logging tool and study the propagation progress of the smoke rings induced in the formation. Additionally, various patents on downhole transient EM measurements for wireline logging, geosteering and ahead of a drill bit have been made internally, comprising the transmitters and receivers, excitation sources, and methods to eliminate the conductive drill string influences of LWD tools etc. (Payton et al., 1999; Mogilatov, 2010; Itskovish, 2017). Although many patents have disclosed the geosteering capability of transient EM logging, basic principle, geosignal definition as well as the detection performances do not exist in the public domain until now.

As we know, an accurate information about the relative dip angle is crucial in geosteering and reservoir evaluation (Hong et al., 2013). Inversion technology has usually been used to extract formation parameters (Gao et al., 2007; Tan et al., 2012; Lai et al., 2018). However, the inversion process often has high calculation complexity and is easily trapped in local minima. Previous studies show that using a multi-frequency focusing (MFF) method can compute the dip and azimuth for frequency-domain measurements (Tabarovsky et al., 2001). Hagiwara (2011) further indicates that the apparent dip from MFF method is less accurate when the formation resistivity is low, the anisotropy is small and the operating frequency is high. Moreover, Hagiwara (2012) also proposes a method to determine the relative dip angle from transient triaxial induction measurements. But how measurement errors would affect the determination result remains unknown.

In this paper, a 401-point digital filtering algorithm of sine/cosine transform is first introduced to calculate the transient multicomponent logging responses. Then, a time-domain geosignal is defined to achieve the directional measurement of formation boundary. Moreover, we find the cross component decays much faster than the coaxial and coplanar components and thereby propose a pseudo-inversion method to determine the dip angle of anisotropic layered formation. The influence of random measurement error on this method is also analyzed. Finally, linear relationship between the DTB and the time corresponding to the half-point of geosignal curves is established to assist in the DTB determination. We hope this study would contribute to the development of the novel transient multicomponent logging measurement.

2. Methodology of transient response calculation

Consider three mutually orthogonal transmitter coils excited by time-harmonic sources, denoted by **M**, we first calculate the frequency-domain multicomponent magnetic fields. The time dependence is assumed to be $e^{-i\omega t}$, Maxwell's equations in unbounded, transverse isotropic (TI) layered medium are expressed as

$$\begin{cases} \nabla \times \mathbf{H} = \overline{\overline{\sigma}}\mathbf{E} \\ \nabla \times \mathbf{E} = i\omega\mu(\mathbf{H} + \mathbf{M}\delta(x,y,z)) \end{cases} \tag{1}$$

where **H** is the magnetic field tensor, **E** is the electric field tensor, μ is the magnetic permeability with $\mu = \mu_0 = 4\pi \times 10^{-7}$H/m, $\delta(x,y,z)$ is a Dirac delta function located at the origin. Since high-frequency components of the EM fields would decay to zero quickly at early time in transient EM surveys, in which case the displacement current can be neglected, the conductivity tensor is found to be

$$\overline{\overline{\sigma}} = \begin{bmatrix} \sigma_h & 0 & 0 \\ 0 & \sigma_h & 0 \\ 0 & 0 & \sigma_v \end{bmatrix} \tag{2}$$

where σ_h is the horizontal conductivity and σ_v is the vertical conductivity.

Frequency-domain magnetic fields excited by z-directed, x-directed and y-directed magnetic dipoles are illustrated as follows. Note that, the azimuth is assumed to be zero in our discussion. Since y-directed transmitter does not couple to the x or z-directed receivers, nor does the y-directed receiver couple to the x or z-directed transmitters, these components are equal to zero.

For a z-directed vertical magnetic dipole in the ith layer of a stratified medium, the magnetic fields in frequency domain are found to be

$$H_{zz}(\omega) = \frac{M_z}{4\pi} \int_0^\infty \left(\frac{\beta_i}{\xi_{hi}} e^{-\xi_{hi}|z-z_0|} + F_i e^{-\xi_{hi}z} + G_i e^{\xi_{hi}z} \right) k_\rho{}^3 J_0(k_\rho\rho)\mathrm{d}k_\rho \tag{3}$$

$$\begin{aligned} H_{zx}(\omega) = \frac{M_z}{4\pi} \int_0^\infty \xi_{hi} \Bigg(\frac{\beta_i}{\xi_{hi}} \frac{|z-z_0|}{z-z_0} e^{-\xi_{hi}|z-z_0|} \\ + F_i e^{-\xi_{hi}z} - G_i e^{\xi_{hi}z} \Bigg) k_\rho{}^2 J_1(k_\rho\rho)\mathrm{d}k_\rho \end{aligned} \tag{4}$$

And for a x-directed horizontal magnetic dipole in ith layer of formation, the magnetic fields in frequency domain are

$$\begin{aligned} H_{xz}(\omega) = \frac{M_x}{4\pi} \int_0^\infty \Bigg(\beta_i \frac{|z-z_0|}{z-z_0} e^{-\xi_{hi}|z-z_0|} \\ + S_i e^{-\xi_{hi}z} + T_i e^{\xi_{hi}z} \Bigg) k_\rho{}^2 J_1(k_\rho\rho)\mathrm{d}k_\rho \end{aligned} \tag{5}$$

Similarly, magnetic fields generated by a y-directed magnetic dipole are derived in the same way, which can be expressed as

$$\begin{aligned} H_{xx}(\omega) = \frac{M_x}{4\pi} \int_0^\infty \left(-\beta_i\xi_{hi}e^{-\xi_{hi}|z-z_0|} - S_i\xi_{hi}e^{-\xi_{hi}z} + T_i\xi_{hi}e^{\xi_{hi}z} \right) k_\rho J_0(k_\rho\rho)\mathrm{d}k_\rho + \\ \frac{M_x}{4\pi\rho} \int_0^\infty \left(\beta_i\xi_{hi}e^{-\xi_{hi}|z-z_0|} + \frac{\beta_i}{\lambda_i\xi_{vi}}k_{hi}{}^2 e^{-\lambda_i\xi_{vi}|z-z_0|} + P_i\frac{k_{hi}{}^2}{\lambda_i}e^{-\lambda_i\xi_{vi}z} + Q_i\frac{k_{hi}{}^2}{\lambda_i}e^{\lambda_i\xi_{vi}z} + S_i\xi_{hi}e^{-\xi_{hi}z} - T_i\xi_{hi}e^{\xi_{hi}z} \right) J_1(k_\rho\rho)\mathrm{d}k_\rho \end{aligned} \tag{6}$$
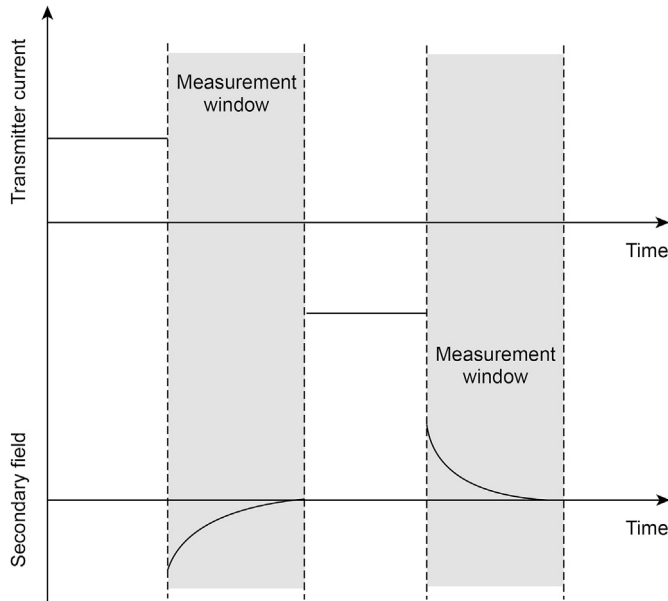
Fig. 1. Basic principle of a TEM logging measurement system.

there is no available result for reference. Consequently, a digital filtering algorithm is finally adopted to achieve the frequency-time conversion in this paper.

Spectrum of a step-on current is

$$I(\omega) = \frac{1}{i\omega} + \pi\delta(\omega) \tag{8}$$

According to the theory of spectrum analysis, time-domain magnetic field $\mathbf{H}(t)$ excited by a step-on current is then obtained by performing Fourier transform

$$\mathbf{H}(t) = \frac{1}{2\pi} \int_{-\infty}^{\infty} \frac{\mathbf{H}(\omega)}{i\omega} e^{i\omega t} d\omega \tag{9}$$

Substitute $\mathbf{H}(\omega) = \mathrm{Re}\mathbf{H}(\omega) - i\mathrm{Im}\mathbf{H}(\omega)$ and $e^{i\omega t} = \cos\omega t + i\sin\omega t$ into equation (9) and we get

$$\mathbf{H}(t) = \frac{1}{2\pi} \int_{-\infty}^{\infty} \left[\frac{\mathrm{Re}\mathbf{H}(\omega)\sin\omega t - \mathrm{Im}\mathbf{H}(\omega)\cos\omega t}{\omega} \right] d\omega$$
$$- \frac{i}{2\pi} \int_{-\infty}^{\infty} \left[\frac{\mathrm{Re}\mathbf{H}(\omega)\cos\omega t + \mathrm{Im}\mathbf{H}(\omega)\sin\omega t}{\omega} \right] d\omega \tag{10}$$

$$H_{yy}(\omega) = \frac{M_y}{4\pi} \int_0^{\infty} \left(\frac{\beta_i}{\lambda_i \xi_{vi}} k_{hi}^2 e^{-\lambda_i \xi_{vi}|z-z_0|} + P_i \frac{k_{hi}^2}{\lambda_i} e^{-\lambda_i \xi_{vi}z} + Q_i \frac{k_{hi}^2}{\lambda_i} e^{\lambda_i \xi_{vi}z} \right) k_\rho J_0(k_\rho\rho) dk_\rho -$$

$$\frac{M_y}{4\pi\rho} \int_0^{\infty} \left(\beta_i \xi_{hi} e^{-\xi_{hi}|z-z_0|} + \frac{\beta_i}{\lambda_i \xi_{vi}} k_{hi}^2 e^{-\lambda_i \xi_{vi}|z-z_0|} + P_i \frac{k_{hi}^2}{\lambda_i} e^{-\lambda_i \xi_{vi}z} + Q_i \frac{k_{hi}^2}{\lambda_i} e^{\lambda_i \xi_{vi}z} + S_i \xi_{hi} e^{-\xi_{hi}z} - T_i \xi_{hi} e^{\xi_{hi}z} \right) J_1(k_\rho\rho) dk_\rho \tag{7}$$

In the expressions above, z_0 and z correspond to the transmitter and receiver position respectively. $\xi_{hi} = (k_\rho^2 - k_{hi}^2)^{1/2}$, $k_{hi} = (i\omega\mu\sigma_{hi})^{1/2}$, $\xi_{vi} = (k_\rho^2 - k_{vi}^2)^{1/2}$, $k_{vi} = (i\omega\mu\sigma_{vi})^{1/2}$, $\lambda_i = \sqrt{\frac{\sigma_{hi}}{\sigma_{vi}}}$, $\beta_i = 1$ or 0, depending on whether the source is in ith layer or not. $J_n(x)$ is the 0/1 order Bessel function. We use the known 120-point J_0 filter and 140-point J_1 filter Hankel transform presented by Guptarsama (1997) to solve the integral above. F_i、G_i、P_i、Q_i、S_i、T_i are calculated with an improved coefficient propagator method proposed by Zhong (2008) and details are not included here. Instead, specific coefficients in a 2-layer medium are present in Appendix A for reference.

Fig. 1 displays the basic principle of a TEM logging measurement system. The transmitter is driven by a 50% duty cycle current wave form. The DC current generates a primary field. Suddenly, abrupt termination of the current resource at time t_0 will induce an electromotive force (emf) and subsequently causes an eddy current in the formation. The eddy current diffuses farther into the formation over time and generates a secondary field. Then, in the receiver, we could measure the time derivatives of magnetic flux vectors, $-dB/dt$, induced by the decaying field.

In order to calculate the time-domain EM fields, Anderson (1989) adopts a 16384-point FFT. Because of the very low computational efficiency, this method usually costs much calculation time. Gaver-Stehfest method is another widely used method in transients (Raiche, 1987). However, the early and late time responses often have large relative errors. Therefore, it is not very suitable for time-domain logging response modeling and analysis, especially when

Based on the parity of frequency-domain magnetic field, the real and imaginary part of $\mathbf{H}(\omega)$ satisfy $\mathrm{Re}[\mathbf{H}(\omega)] = \mathrm{Re}[\mathbf{H}(-\omega)]$ and $\mathrm{Im}[\mathbf{H}(\omega)] = -\mathrm{Im}[\mathbf{H}(-\omega)]$. Equation (10) is simplified to

$$\mathbf{H}(t) = \frac{1}{\pi} \int_0^{\infty} \left[\frac{\mathrm{Re}\mathbf{H}(\omega)\sin\omega t - \mathrm{Im}\mathbf{H}(\omega)\cos\omega t}{\omega} \right] d\omega \tag{11}$$

In geologic applications, we usually measure the response excited by a step-off current. And the time-domain magnetic field excited by a step-off current can be calculated from a step-on response

$$\mathbf{H}(t) = \mathbf{H}(\infty) - \frac{1}{\pi} \int_0^{\infty} \left[\frac{\mathrm{Re}\mathbf{H}(\omega)\sin\omega t - \mathrm{Im}\mathbf{H}(\omega)\cos\omega t}{\omega} \right] d\omega \tag{12}$$

Since the secondary field equals to zero when $t < 0$, replace t by $-t$ in the above formula

$$0 = -\frac{1}{\pi} \int_0^{\infty} \left[\frac{-\mathrm{Re}\mathbf{H}(\omega)\sin\omega t - \mathrm{Im}\mathbf{H}(\omega)\cos\omega t}{\omega} \right] d\omega \tag{13}$$

If equation (12) minus by equation (13):

$$\mathbf{H}(t) = \frac{2}{\pi} \int_0^\infty \left[\frac{\mathrm{Im}\mathbf{H}(\omega)\cos \omega t}{\omega} \right] \mathrm{d}\omega \tag{14}$$

and if equation (12) plus equation (13):

$$\mathbf{H}(t) = -\frac{2}{\pi} \int_0^\infty \left[\frac{\mathrm{Re}\mathbf{H}(\omega)\sin \omega t}{\omega} \right] \mathrm{d}\omega \tag{15}$$

From equations (14) and (15) we know that either the real or the imaginary part of $\mathbf{H}(\omega)$ can be used alone to calculate $\mathbf{H}(t)$.

According to Faraday's Law, the voltage $\mathbf{V}(t)$ excited by a step-off current can be expressed by

$$\mathbf{V}(t) = \frac{2NS\mu}{\pi} \int_0^\infty \mathrm{Im}(\mathbf{H}(\omega))\sin \omega t\mathrm{d}\omega \tag{16}$$

and

$$\mathbf{V}(t) = \frac{2NS\mu}{\pi} \int_0^\infty \mathrm{Re}(\mathbf{H}(\omega))\cos \omega t\mathrm{d}\omega \tag{17}$$

where N is the number of coils, S is the coil area.

Now we need to solve the infinite integral of the sine or cosine functions above. Based on the relations between Bessel functions and sine/cosine functions

$$\sin(\omega t) = \sqrt{\frac{\pi\omega t}{2}}J_{1/2}(\omega t) \;, \cos(\omega t) = \sqrt{\frac{\pi\omega t}{2}}J_{-1/2}(\omega t) \tag{18}$$

the integral of high oscillating functions equations (16) and (17) are transformed to the integral of first kind and $\pm 1/2$ order Bessel function

$$\mathbf{V}(t) = NS\mu\sqrt{\frac{2}{\pi t}} \int_0^\infty \frac{\mathrm{Im}(\mathbf{H}(\omega))}{\sqrt{\omega}} \omega J_{1/2}(\omega t)\mathrm{d}\omega \tag{19}$$

$$\mathbf{V}(t) = NS\mu\sqrt{\frac{2}{\pi t}} \int_0^\infty \frac{\mathrm{Re}(\mathbf{H}(\omega))}{\sqrt{\omega}} \omega J_{-1/2}(\omega t)\mathrm{d}\omega \tag{20}$$

Using Hankel integral transforms, equations (19) and (20) can be calculated from these two expressions

$$\begin{aligned}\mathbf{V}(t) &= NS\mu\sqrt{\frac{2}{\pi t^2}} \sum_{n=-\infty}^{+\infty} \mathrm{Im}(\mathbf{H}(e^{n\Delta}/t)) \cdot \sqrt{e^{n\Delta}} \cdot H_{1/2}(n\Delta) \\ &= NS\mu\sqrt{\frac{2}{\pi t^2}} \sum_{n=-\infty}^{+\infty} \mathrm{Im}(\mathbf{H}(e^{n\Delta}/t)) \cdot c\sin(n\Delta)\end{aligned} \tag{21}$$

and

$$\begin{aligned}\mathbf{V}(t) &= NS\mu\sqrt{\frac{2}{\pi t^2}} \sum_{n=-\infty}^{+\infty} \mathrm{Re}(\mathbf{H}(e^{n\Delta}/t)) \cdot \sqrt{e^{n\Delta}} \cdot H_{-1/2}(n\Delta) \\ &= NS\mu\sqrt{\frac{2}{\pi t^2}} \sum_{n=-\infty}^{+\infty} \mathrm{Re}(\mathbf{H}(e^{n\Delta}/t)) \cdot c\cos(n\Delta)\end{aligned} \tag{22}$$

where $H_{\pm 1/2}(n\Delta)$ is the digital filter weights for Hankel $J_{\pm 1/2}$ transform; Δ is the sampling interval; $c\sin(n\Delta)$ and $c\cos(n\Delta)$ are defined as the sine and cosine filter weights respectively. Here we
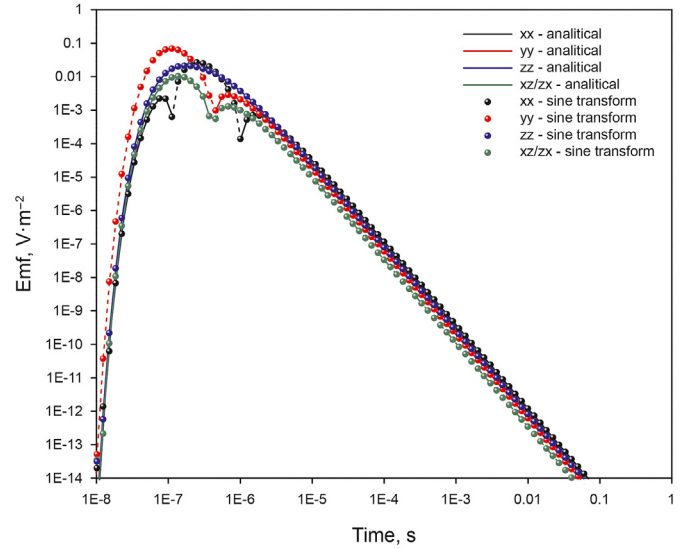

Fig. 2. Validation of the transient multicomponent EM response calculation. The spacing is 96 in. The relative dip angle $\alpha = 60°$. The horizontal resistivity $R_{\mathrm{h}} = 2\ \Omega\cdot\mathrm{m}$ and the vertical resistivity $R_{\mathrm{v}} = 8\ \Omega\cdot\mathrm{m}$.

adopt $\Delta = \ln(10)/20$, design 401-point $(-200-200)$ $J_{\pm 1/2}$ filter weights and the corresponding sine/cosine filters (Johansen, 1979; Wang, 2004). Then, all conditions for calculating equations (18) and (19) are prepared.

Substituting equations (3), (4), (5), (6), (7) into equation (21) or (22), voltage tensor of transient multicomponent EM logging in the formation coordinate system can be obtained, which is supposed to be

$$\mathbf{V} = \begin{bmatrix} V_{xx}(t) & 0 & V_{xz}(t) \\ 0 & V_{yy}(t) & 0 \\ V_{zx}(t) & 0 & V_{zz}(t) \end{bmatrix} \tag{23}$$

When the dip angle is α, we need to transform the transient triaxial responses in the formation (x,y,z) system to the sonde system (x',y',z'). Tensor voltage in these two coordinate systems are related by an axis rotation matrix expressed by

$$\mathbf{V}' = \mathbf{R}^{-1}V\mathbf{R} \tag{24}$$

where $\mathbf{R}$ is the rotation matrix:

$$\mathbf{R} = \begin{bmatrix} \cos \alpha & 0 & \sin \alpha \\ 0 & 1 & 0 \\ -\sin \alpha & 0 & \cos \alpha \end{bmatrix} \tag{25}$$

In this way, transient multicomponent EM logging responses of an arbitrary orientated instrument in transverse isotropic formation can be quickly calculated.

3. Forward modeling

3.1. Validation

A homogenous, unbounded, TI medium is firstly considered here to verify the calculation results. Note that there exist analytical expressions of transient multicomponent EM logging responses in homogenous TI formation. Detailed derivations are given in Appendix B.

Fig. 2 presents the calculation results from the analytical expressions in Appendix B and the sine transform digital filtering algorithm of equation (21). Agreement between the analytical and
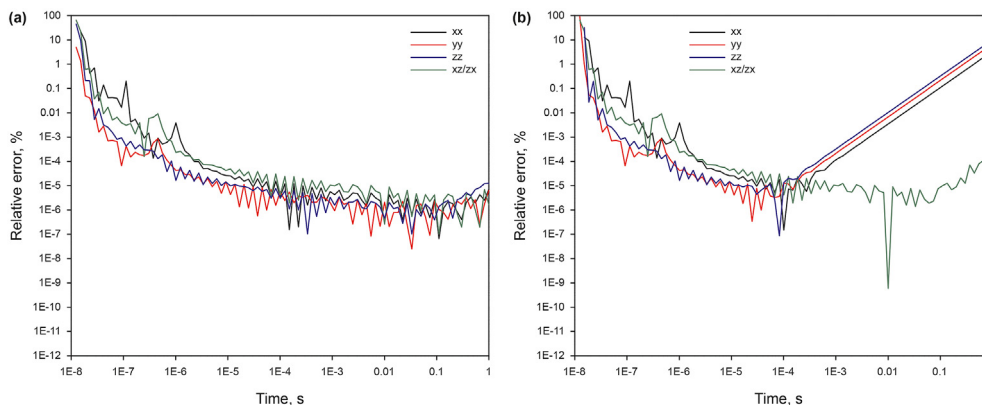
Fig. 3. Relative errors of these two digital filtering algorithms. (a) Relative error of the sine transform digital filtering; (b) relative error of the cosine transform digital filtering.

semi-analytical results is excellent, indicating that our codes are effective. The solid and dash line correspond to positive and negative value respectively, and absolute value is taken in plotting. Extreme point between them is called the 'zero-crossing' point in transient surveys. It should be noteworthy that all components measured in the sonde coordinate system have the typical $t^{-5/2}$ decay at late times.

We also compare the calculation results with equation (21) and equation (22). Model parameters are the same as Fig. 2. Fig. 3 displays the relative errors produced by these two semi-analytical methods. Early-time emfs mainly correspond to the integral of high-frequency magnetic fields, and the relative errors are very large. However, magnitude of these emfs is small and high-frequency EM fields would decay to zero quickly, so we approximately ignore this impact. Except for the very early times, these two methods show good accuracy.

Moreover, relative errors calculated by cosine transform are several orders higher than the sine transform at late times, especially for the coaxial and coplanar components, whose errors linearly increase. After converting the sine/cosine integrals into Hankel $J_{\pm 1/2}$ transform, the calculation results are closely related to the filter parameters. This phenomenon indicates that the $J_{1/2}$ filters are more suitable than the $J_{-1/2}$ for solving late-time emfs.

Therefore, all the following simulations adopt the sine transform rather than the cosine transform digital filtering.

3.2. Boundary detection performance

To detect the formation boundary, refer to the boundary mode

of the frequency-domain ultra-deep directional resistivity measurements (Seydoux et al., 2014), the time-domain geosignal of transient multicomponent EM logging measurement is defined to be

$$\text{Geosignal}(t) = 20 \log_{10} \left| \frac{V_{zz}(t) - V_{zx}(t)}{V_{zz}(t) + V_{zx}(t)} \cdot \frac{V_{zz}(t) + V_{xz}(t)}{V_{zz}(t) - V_{xz}(t)} \right| \quad (26)$$

By referring to the noise threshold that used in the frequency-domain directional logging, maximum DOD is evaluated. We define the threshold as 0.25 dB, which means geosignals greater than 0.25 dB are attributed to the influence of bed boundary. To study the boundary detection performance, a 2-layer formation model is considered, in which the tool is parallel to the formation boundary, as displayed by Fig. 4.

Fig. 5 displays the boundary detection performances with different resistivity contrast. At early times before the eddy current reaches the interface, geosignal reads zero. Geosignal appears when transient EM measurements start 'seeing' the boundary. Since the eddy current diffuses away from the boundary and farther into the shoulder bed as time progresses, geosignal gradually decreases to zero at late time. We can make several key observations on Fig. 5: (1) The boundary detection measurement equals to zero when the eddy current is far away from the resistivity interface; (2) DOD of this time-domain EM measurement can reach tens of meters; (3) geosignal presents positive values in a resistive layer and negative values in a conductive layer; (4) same resistivity contrast almost corresponds to the same measurements but the boundary is sensed earlier as the formation resistivity increases, that is because the eddy current diffuses faster in high-resistivity formation; (5)
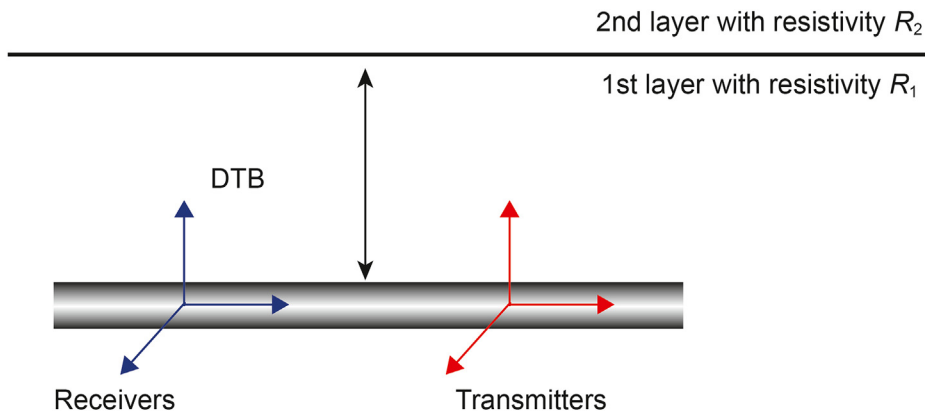

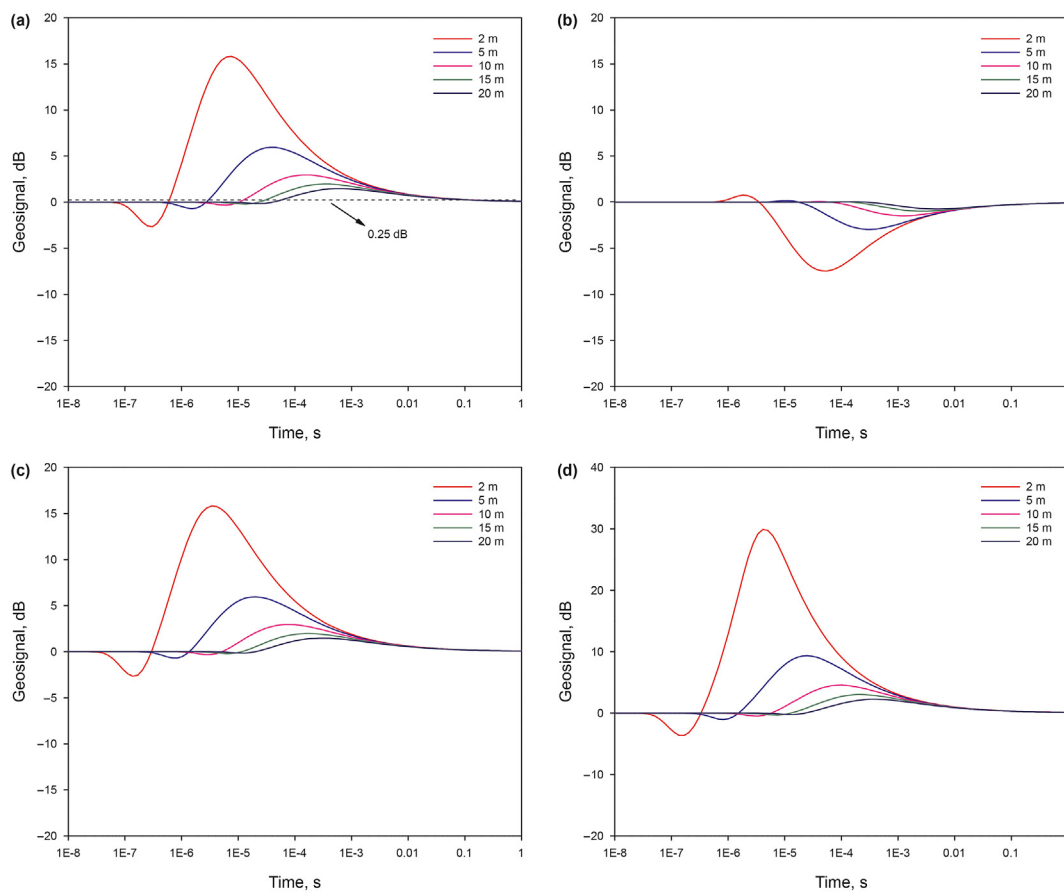**Fig. 4.** 2-layer DOD model. The spacing is 96 in.

Fig. 5. Boundary detection performances of transient multicomponent EM LWD method. (a) $R_1 = 10\ \Omega \cdot m$ and $R_2 = 1\ \Omega \cdot m$; (b) $R_1 = 1\ \Omega \cdot m$ and $R_2 = 10\ \Omega \cdot m$; (c) $R_1 = 20\ \Omega \cdot m$ and $R_2 = 2\ \Omega \cdot m$; (d) $R_1 = 20\ \Omega \cdot m$ and $R_2 = 1\ \Omega \cdot m$.

detection capability in a resistor is more excellent than in a conductor and higher resistivity contrast results to a larger geosignal. Compared to the time-harmonic measurements, transient EM logging greatly enhance the DOD.

3.3. Dip angle effect

Consider a 2-layer model, as shown in Fig. 6, α indicates the relative dip angle. From Fig. 7 it can be found that the time-domain
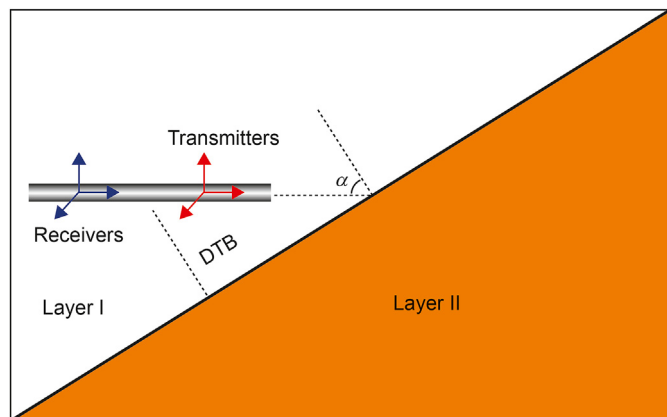
Fig. 6. 2-layer formation model.

geosignal increases with an increasing dip angle. However, when the dip is greater than 80°, the increase is not obvious. Moreover, the peak and the half point of the curve both slightly move towards the positive direction of the time axis when the dip increases.

3.4. Anisotropy effect

To study the anisotropic effect on measured geosignals, take the model in Fig. 4 as example, Layer I and Layer II are considered to be anisotropic respectively.

Fig. 8 presents the case when Layer I is anisotropic and Layer II is isotropic. If the horizontal resistivity remains the same and the vertical resistivity increases, as shown in Fig. 8(a), geosignal increases and the peak moves to the left. On the contrary, if the vertical resistivity remains the same and the vertical resistivity increases, compared to Fig. 8(a), increase of the curve in Fig. 8(b) is more obvious.

When Layer I is isotropic and Layer II is anisotropic, as shown in Fig. 9, with the change of vertical resistivity of the anisotropic shoulder, curves almost present the same value. However, if the horizontal resistivity increases, geosignals drop sharply due to the decrease of resistivity contrast. This interesting phenomenon indicates that anisotropy from the shoulder has very little effect on the boundary detection performance.

In summary, anisotropy of the layer where the tool is located must be taken into consider, while the shoulder bed can almost be regarded as isotropic.
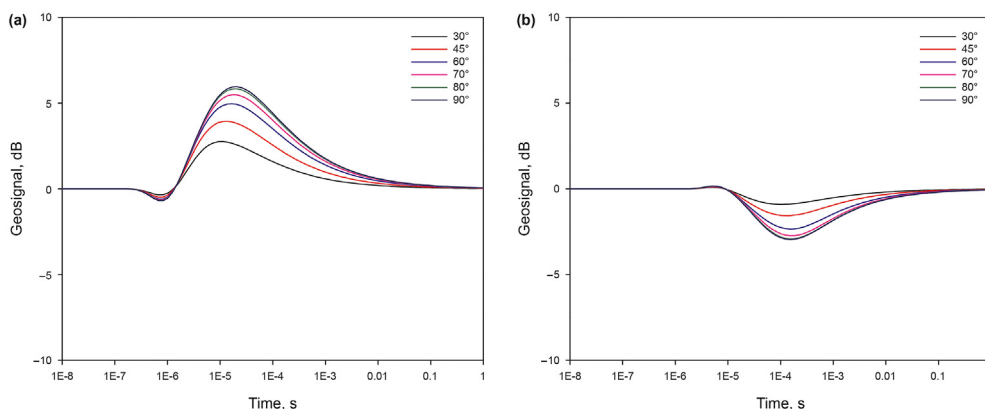
Fig. 7. Boundary detection performances with different relative dip angles. The spacing is 96 in. DTB = 5 m. (a) $R_1 = 20\ \Omega \cdot \text{m}$, $R_2 = 2\ \Omega \cdot \text{m}$; (b) $R_1 = 2\ \Omega \cdot \text{m}$, $R_2 = 20\ \Omega \cdot \text{m}$.
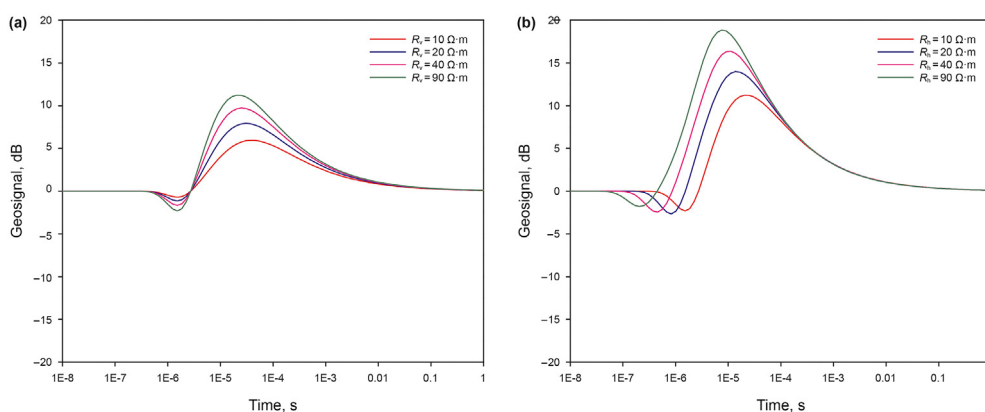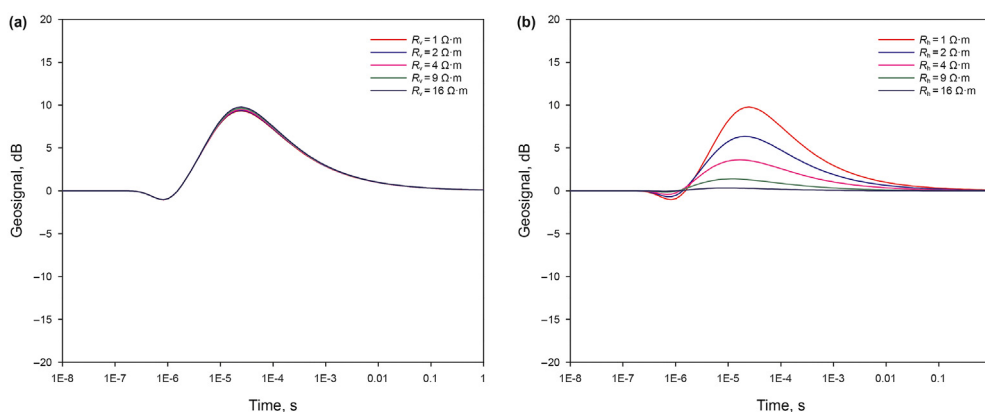

Fig. 8. Boundary detection performances in anisotropic formation. The spacing is 96 in. DTB = 5 m. Layer I is anisotropic and Layer II is isotropic, $R_2 = 1\ \Omega \cdot \text{m}$. (a) R_h of Layer I is 10 $\Omega \cdot \text{m}$ and R_v of Layer I are 10, 20, 40, 90 $\Omega \cdot \text{m}$ respectively; (b) R_v of Layer I is 90 $\Omega \cdot \text{m}$ and R_h of Layer I are 10, 20, 40, 90 $\Omega \cdot \text{m}$ respectively.

Fig. 9. Boundary detection performances with anisotropic shoulder bed. The spacing is 96 in. DTB = 5 m. Layer II is anisotropic and Layer I is isotropic, $R_1 = 20\ \Omega \cdot \text{m}$. (a) R_h of Layer II is 1 $\Omega \cdot \text{m}$ and R_v of Layer II are 1, 2, 4, 9, 16 $\Omega \cdot \text{m}$ respectively; (b) R_v of Layer II is 16 $\Omega \cdot \text{m}$ and R_h of Layer II are 1, 2, 4, 9, 16 $\Omega \cdot \text{m}$ respectively.

3.5. Directional capability

This transient multicomponent EM logging method is capable of producing time-domain directional measurements. Fig. 10 presents two typical cases in which it is crucial to control the well trajectory. Geosteering decisions to drill above or below are essential for successful well planning. Fig. 11 gives the corresponding measurements to these two cases with dip angles of 30, 45, 60, 90° respectively. The solid line and the dash line correspond to the tool below or above the boundary respectively. Polarity of the signal reverses depending on whether a conductive bed is approached from above or below. When the transient tool is located below a conductive bed, the geosignals are positive. Oppositely, a negative signal is obtained when the tool is placed above. Thus, the polarity can assist in making geosteering decisions, e.g. maintain the borehole trajectory in reservoir or avoid drilling risks by steer up or down.
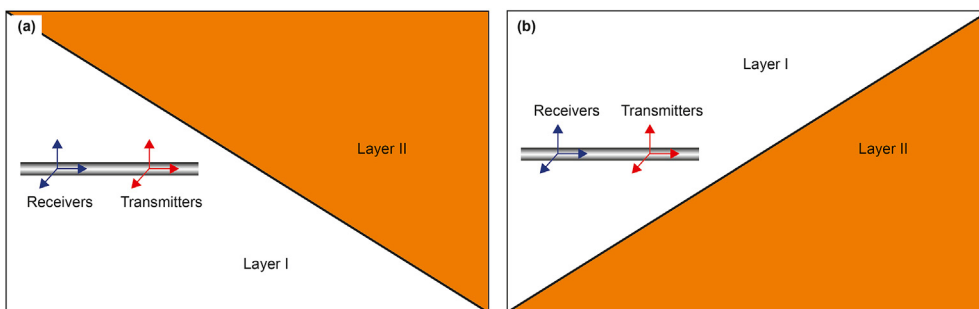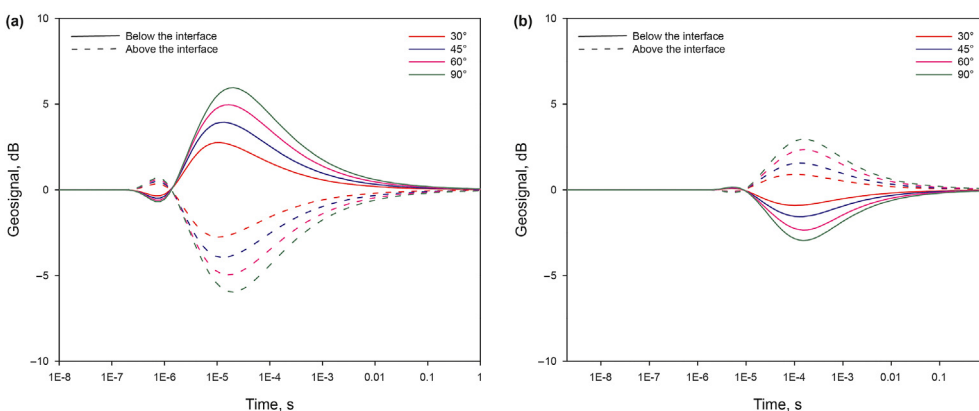
Fig. 10. Directional measurement models.

Fig. 11. Directional measurements. The tool is placed in layer I. The spacing is 96 in. DTB = 5 m. (a) $R_1 = 20$ Ω·m, $R_2 = 2$ Ω·m; (b) $R_1 = 2$ Ω·m, $R_2 = 20$ Ω·m.
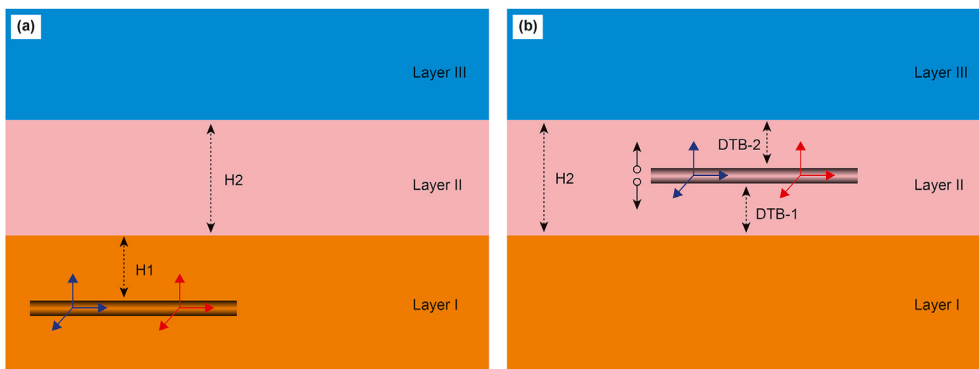

Fig. 12. 3-layer model.

3.6. 3-Layer model

Fig. 12 presents two cases of 3-layer model. In Fig. 12(a), the transient tool is located at Layer I and distance to the first interface H1 is 2 m. Fig. 13 displays the corresponding geosignal curves with different H2. Moreover, a 2-layer model is also included for reference, which means Layer II and Layer III have the same resistivity, indicated by the red solid line. At early times, these curves are completely overlapped; when eddy current encounters the second interface, geosignal curve start separated from the 2-layer curve. If Layer III is a resistor, as shown in Fig. 13(a), the responses deviate downward from the 2-layer curve. If Layer III is a conductor, as shown in Fig. 13(b), curves of the 3-layer model deviate upward and another peak appears. The time when the deviation occurs depends on the thickness of Layer II.

When the tool is placed in Layer II, as shown in Fig. 12(b), the thickness of Layer II is 10 m. DTB-1 and DTB-2 stands for the distance to the first and second boundary respectively. Fig. 14 presents the corresponding geosignal measurements. The black solid line indicates the case when the tool is located at the center of layer II (DTB-1 = DTB-2). Response should be regarded as the contributions from these two boundaries, so geosignal reads zero all the period in case of the azimuthal sensitivity. ±1/2 m means some shift above or below the center. For example, +2 m corresponds to the case when the tool moves up 2 m (DTB-1 = 7 m; DTB-2 = 3 m): If Layer II is a resistor, since positive geosignal from the second boundary increases and negative geosignal from the first boundary decreases, the measurement presents a positive value; if Layer II is a conductor, on the contrary, the measurement presents a negative value. Certainly, when the tool moves downward 2 m (DTB-1 = 3 m,
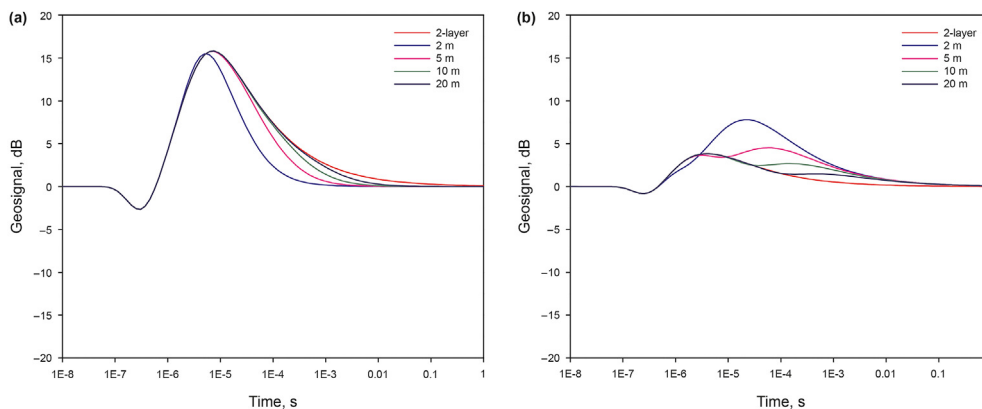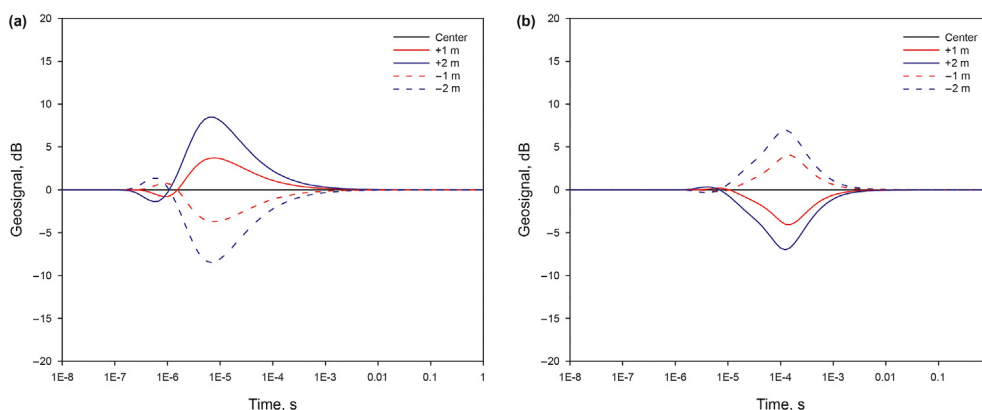
Fig. 13. Boundary detection performances in a 3-layer model when the tool is placed in Layer I. The spacing is 96 in. H1 = 2 m. (a) $R_1 = 10\ \Omega\cdot m$, $R_2 = 1\ \Omega\cdot m$, $R_3 = 10\ \Omega\cdot m$; (b) $R_1 = 10\ \Omega\cdot m$, $R_2 = 4\ \Omega\cdot m$, $R_3 = 1\ \Omega\cdot m$.

Fig. 14. Boundary detection performances in a 3-layer model when the tool is placed in Layer II. The spacing is 96 in. H2 = 10 m. (a) $R_1 = 1\ \Omega\cdot m$, $R_2 = 10\ \Omega\cdot m$, $R_3 = 1\ \Omega\cdot m$; (b) $R_1 = 10\ \Omega\cdot m$, $R_2 = 1\ \Omega\cdot m$, $R_3 = 10\ \Omega\cdot m$.

DTB-2 = 7 m), amplitude of the curve is equal but with opposite polarity.

4. Pseudo-inversion for the determination of dip angle and DTB

Fig. 15 presents a typical simplified model in well placement. DTB and the dip angle α are two key factors in making geosteering decisions. Following we will discuss how to process the transient multicomponent EM measurements to obtain α and DTB.

From equation (24), it can be derived that there are following relations exist from the formation and sonde coordinate systems

$$V'_{zz} - V'_{xx} = \left(\cos^2\alpha - \sin^2\alpha\right)(V_{zz} - V_{xx}) + 2\sin\alpha\cos\alpha(V_{zx} + V_{xz})$$
$$V'_{xz} + V'_{zx} = \left(\cos^2\alpha - \sin^2\alpha\right)(V_{zx} + V_{xz}) + 2\sin\alpha\cos\alpha(V_{xx} - V_{zz})$$
$$V'_{zz} + V'_{xx} = V_{zz} + V_{xx}$$

$$(27)$$

Therefore,

$$\frac{V'_{xz} + V'_{zx}}{V'_{zz} - V'_{xx}} = -\frac{\tan 2\alpha - \frac{V_{xz}+V_{zx}}{V_{zz}-V_{xx}}}{1 + \tan 2\alpha \frac{V_{xz}+V_{zx}}{V_{zz}-V_{xx}}} = -\tan(2\alpha + 2\psi) \qquad (28)$$

where $\tan 2\psi = -\frac{V_{xz}+V_{zx}}{V_{zz}-V_{xx}}$. As long as $\tan(2\psi) = 0$, the apparent dip can be algebraically determined by equation (28). It should be

noteworthy that this pseudo-inversion method cannot be used for frequency-domain measurements because of the non-zero $\tan(2\psi)$.

Fig. 16 displays the transient multicomponent voltages of a homogenous TI medium in the formation coordinate system. Late-time decay of the cross component is proportional to $t^{-7/2}$ and the coaxial/coplanar components have the typical $t^{-5/2}$ decay, making $\tan(2\psi) = 0$ at some particular moments. Then the apparent dip of anisotropic medium could be determined accurately by

$$\tan(2\alpha_{app}) \approx -\frac{V'_{xz} + V'_{zx}}{V'_{zz} - V'_{xx}} \qquad (29)$$

where α_{app} is the apparent dip angle.

For the dip determination simulation, we carry out the forward modeling results and then use equation (29) to algebraically calculate the apparent dip. A homogenous anisotropic formation with different original dip angles is firstly considered to test the effectiveness. From Fig. 17, it is obvious that the results are excellent theoretically. The apparent dip equals to the true dip at early times. It then goes through a sharp transition deviating from the true value and gradually approaches to the true dip again at late times. Moreover, it is easier to determine the dip in a high angle well than in a low angle well because the transition time is much shorter.

When it comes to a stratified formation, three cases are considered here: Layer I is isotropic while Layer II is anisotropic; Layer I is anisotropic while Layer II is isotropic; both Layer I and II are anisotropic. If the transient tool is placed in the isotropic layer,
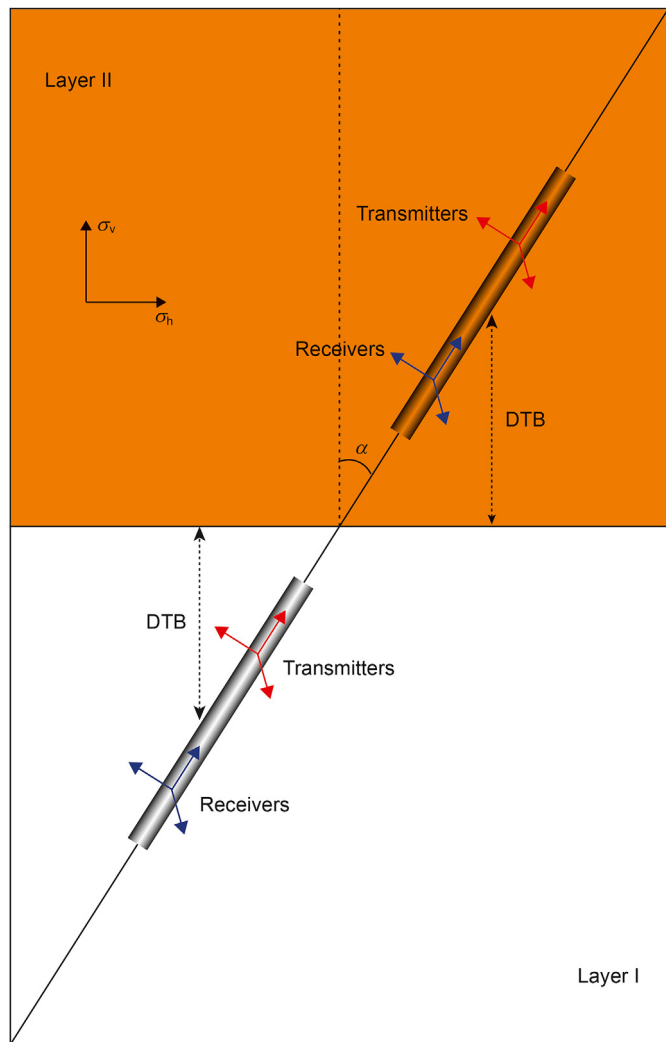
Fig. 15. A simplified 2-layer model.

Fig. 17. Dip determination in homogenous TI formation with different original dip angles. The spacing is 96 in. $R_h = 2\ \Omega\cdot m$ and $R_v = 8\ \Omega\cdot m$.

current would diffuse farther into the anisotropic shoulder. Thus, the measured cross component comes from two aspects: the boundary and the anisotropy, resulting the apparent dips presenting a sharp variation. At late times, it gradually approaches to the true dip. Different DTB corresponds to different time when the apparent dip changes from zero to the true dip. Fig. 19(a) shows the case in which the tool is placed in the anisotropic layer with an isotropic shoulder. The apparent dip curve is similar to that in a homogenous anisotropic formation. Different DTBs almost correspond to the same apparent dip. Effect of DTB is not observed clearly on the apparent dips. If both layers are anisotropic, as shown in Fig. 20(a), it is similar to the second case.

In order to investigate the practicality of this algebraic method, different percentages of random measurement error are added to the modeling results to simulate the actual measured signal as much as possible. We then process these transient multicomponent logging data to calculate the dip. As shown in Fig. 18(b), (c), Fig. 19(b), (c) and Fig. 20(b), (c), the dip determination is stable and the relative error is controlled in an acceptable range, proving the practicality of this pseudo-inversion method. It can be inferred that as long as one anisotropic layer is included in the formation, we can

the dip determination results are shown in Fig. 18(a). At early times, eddy current diffuses in the isotropic layer and the measured cross component equals to zero, so apparent dip angles read zero as well. During the transition times, when eddy current encounters the boundary, the cross component becomes non-zero; next, the eddy
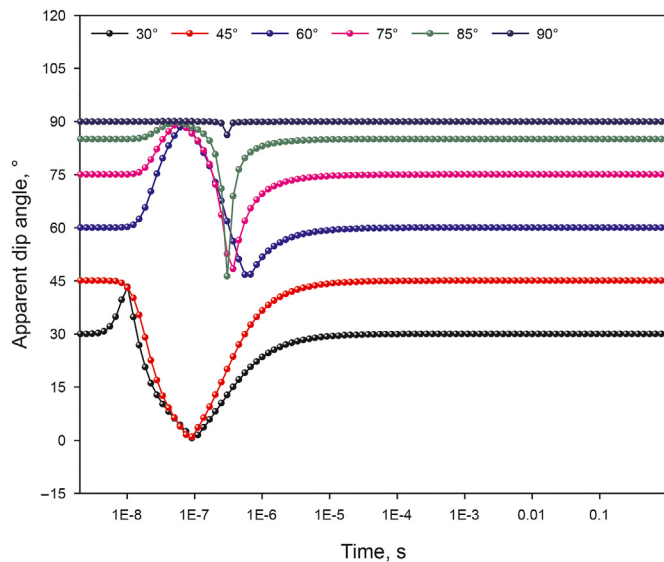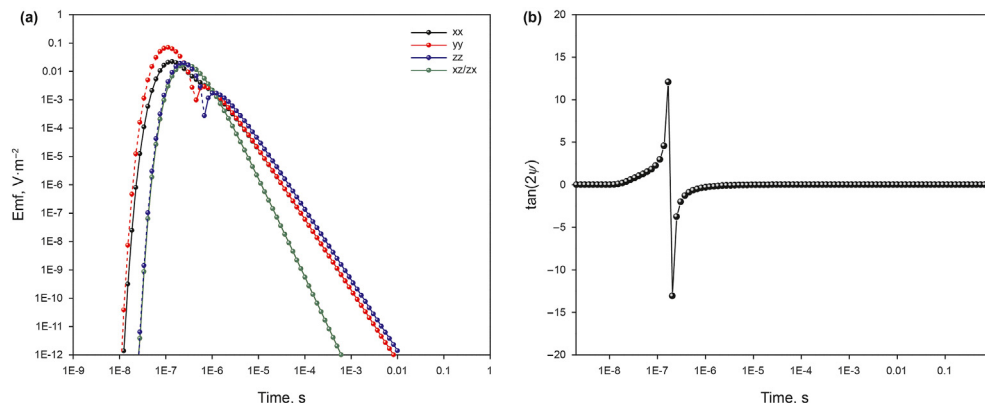

Fig. 16. Transient multicomponent responses in formation coordinate system. The spacing is 96 in. The relative dip angle $\alpha = 60°$. $R_h = 2\ \Omega\cdot m$ and $R_v = 8\ \Omega\cdot m$. (a) Multicomponent voltages; (b) time-domain $\tan(2\psi)$.
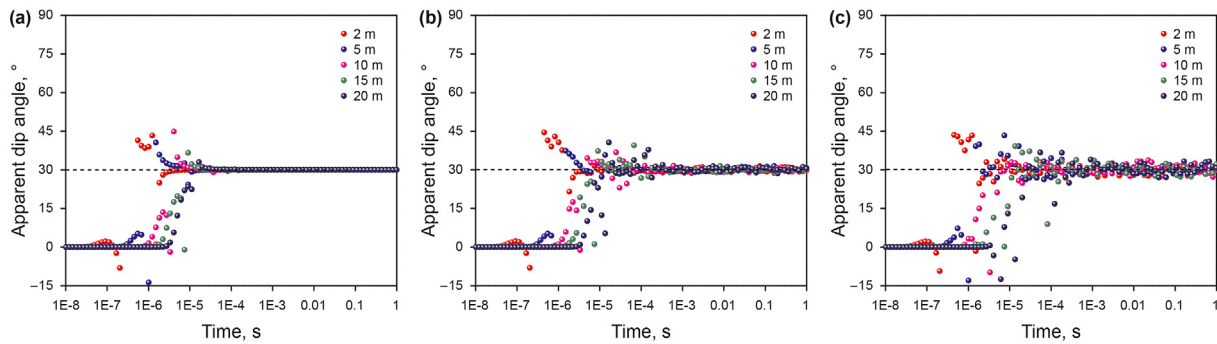
Fig. 18. Dip determination in a 2-layer model with different DTB. Layer I is isotropic and layer II is anisotropic, resistivity of Layer I is 20 Ω·m, R_h and R_v of Layer II are 1 Ω·m and 4 Ω·m respectively. (a) Theoretical results; (b) consider 2% random measurement error; (c) consider 5% random measurement error.
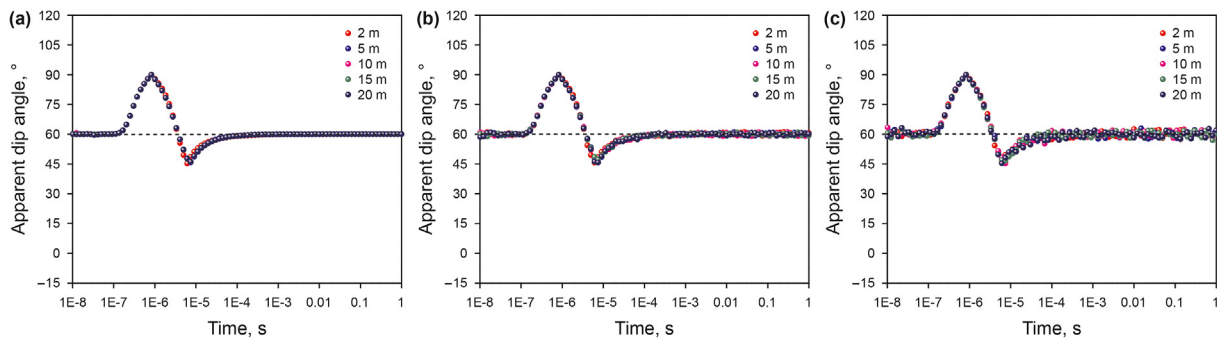

Fig. 19. Dip determination in a 2-layer model with different DTB. Layer I is anisotropic and layer II is isotropic, R_h and R_v of Layer I are 1 Ω·m and 4 Ω·m respectively, resistivity of Layer II is 20 Ω·m. (a) Theoretical results; (b) consider 2% random measurement error; (c) consider 5% random measurement error.
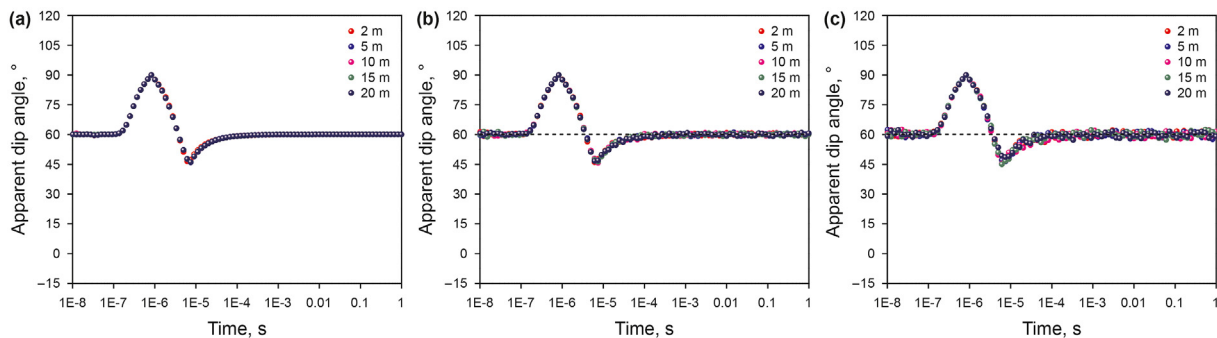

Fig. 20. Dip determination in a 2-layer model with different DTB. Both layer I and layer II are anisotropic, R_h and R_v of layer I are 1 Ω·m and 4 Ω·m respectively, R_h and R_v of Layer II are 2 Ω·m and 20 Ω·m respectively. (a) Theoretical results; (b) consider 2% random measurement error; (c) consider 5% random measurement error.

use this method to algebraically determine the relative dip. But it would fail to process transient multicomponent voltages in pure isotropic layers.

To determine the DTB, we plot the DTBs and the moments at which the half-point of the geosignal curve appears. As shown in Fig. 21(a)-(d), there are linear relationships between DTBs and the half-point time. The DTB determination mainly depends on the layer at which the tool is located. Transient EM wave propagates faster in a resistive bed than in a conductive bed. Thus, it takes shorter time to detect the boundary in a larger resistivity formation. Compared to the resistivity, the dip has relatively small effect on the time we measured the boundary. In processing transient measurements, when the boundary indication appears, the DTB can be quickly determined through this way.

5. Conclusions

In this paper, both 401-point sine transform and cosine transform digital filtering algorithms are adopted to calculate the transient multicomponent voltages. The sine transform works much better than the cosine transform in calculating late-time responses.

By defining a time-domain geosignal, this novel multicomponent EM logging method is capable of detecting formational boundary within tens of meters, including directionally measurements.

Typical characteristic that the time-domain cross component decays much faster than the coaxial/coplanar components in the formation coordinate system offers an opportunity to use pseudo-inversion method to calculate the dip. But this algebraic method
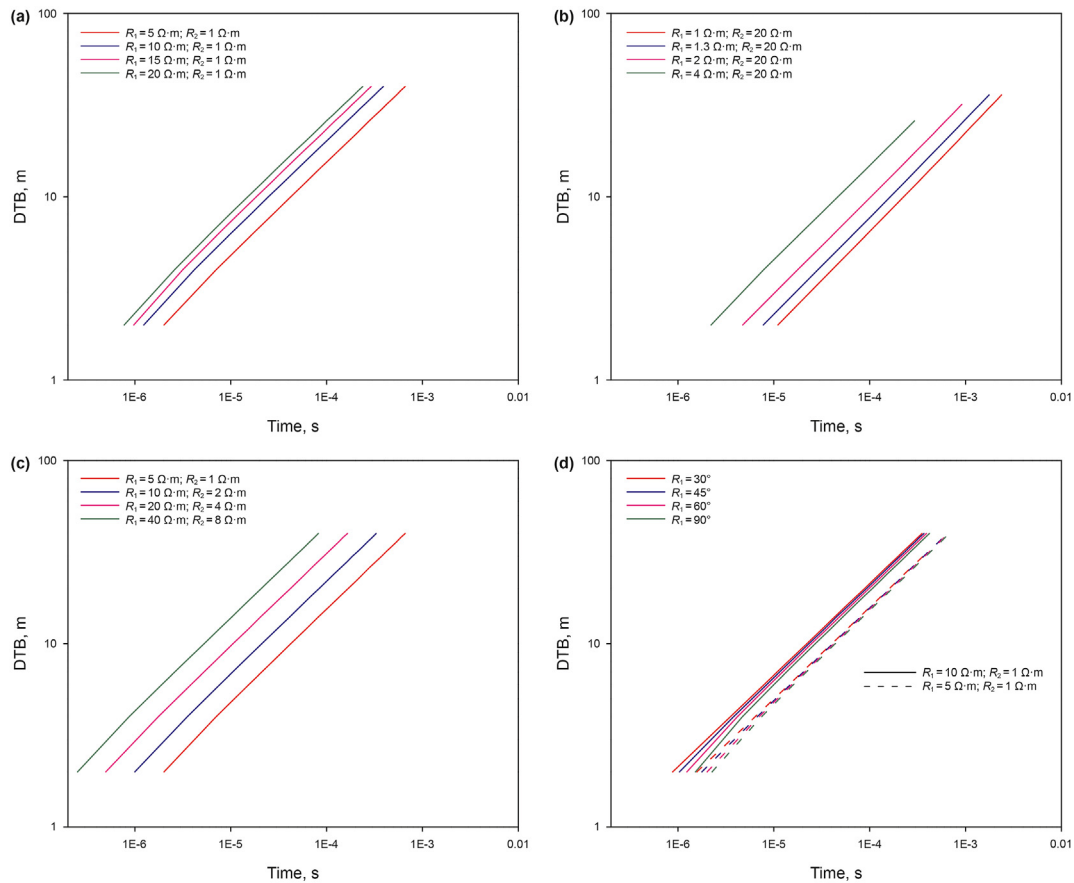
Fig. 21. Determination of DTB. The dip of (a), (b), (c) is 60°. In (d), resistivity of Layer I is 10 and 5 Ω·m respectively, resistivity of Layer II is 1 Ω·m. (a) The tool is placed in a sandstone with different resistivity; (b) The tool is placed in a shale with different resistivity; (c) The tool is placed in a sandstone with the same resistivity contrast; (d) with different dip angles.

requires the formation to be anisotropic or include at least one anisotropic layer. That is, it fails to process the measurements in pure isotropic layers.

We have studied the boundary detection performances of transient multicomponent EM logging measurement. Another factor we are concerned about while drilling is the formation resistivity. Also, the boundary detection performances are closely related to the resistivity as well. So, it is necessary to work on the extraction of formation resistivity from transient multicomponent logging responses in the future study.

Acknowledgements

Appendix A

Coefficients of the Frequency-domain Magnetic Field in a 2-layer TI Medium

Firstly, for a *z*-directed time-harmonic vertical magnetic dipole,

there exists $F_1 = G_2 = 0$ and we only need to derive F_2 and G_1 according to the continuity of EM fields at the interface $z = 0$, which can be expressed by

$$F_2 = \frac{2m_1 - x_{12}m_2}{x_{11}} \tag{A1}$$

$$G_1 = \frac{y_{11}m_2 + y_{12}F_2}{2} \tag{A2}$$

where

$$x_{11} = \frac{\mu_2}{\mu_1} + \frac{\xi_{h2}}{\xi_{h1}}, \; x_{12} = \frac{\mu_2}{\mu_1} - \frac{\xi_{h2}}{\xi_{h1}}$$

$$y_{11} = \left(\frac{\mu_2}{\mu_1} + \frac{\xi_{h2}}{\xi_{h1}}\right), \; y_{12} = \left(\frac{\mu_2}{\mu_1} - \frac{\xi_{h2}}{\xi_{h1}}\right)$$

$$m_1 = \frac{\beta_1}{\xi_{h1}}e^{\xi_{h1}z_0}, \; m_2 = \frac{\beta_2}{\xi_{h2}}e^{-\xi_{h2}z_0}$$

Secondly, for a *x*-directed time-harmonic vertical magnetic dipole, there exists $P_1 = S_1 = Q_2 = T_2 = 0$, and other coefficients are found to be

$$P_2 = \frac{2m'_1 - x'_{12}m'_2}{x'_{11}} \tag{A3}$$

$$Q_1 = \frac{y'_{11}m'_2 + y'_{12}P_2}{2} \tag{A4}$$

where

$$x'_{11} = \frac{\lambda_1}{\lambda_2}\frac{k_{h2}{}^2}{k_{h1}{}^2} + \frac{\mu_2}{\mu_1}\frac{\xi_{v2}}{\xi_{v1}}, \ x'_{12} = \frac{\lambda_1}{\lambda_2}\frac{k_{h2}{}^2}{k_{h1}{}^2} - \frac{\mu_2}{\mu_1}\frac{\xi_{v2}}{\xi_{v1}}$$

Substitute the coefficients above into the frequency-domain magnetic field expressions, magnetic fields at any depth in a 2-layer model can be quickly calculated.

Appendix B

Time-domain Multicomponent Voltages in a Homogenous TI Medium

Following Moran and Gianzero (1979), we first derived the expressions for the frequency-domain magnetic field tensor $\mathbf{H}(\omega)$ in TI medium. Magnetic field components at the receiver in formation coordinate (x,y,z) system can be expressed by

$$
\begin{aligned}
H_{xx}(\omega) &= -\frac{1}{4\pi}\left(\frac{ik_h}{L^2\sin^2\alpha}\right)e^{ik_v\xi} - \frac{1}{4\pi}e^{ik_hL}\left[-\frac{ik_h}{L^2\sin^2\alpha} + \frac{(\sin^2\alpha-1)k_h^2}{L} + \frac{(3\sin^2\alpha-1)ik_h}{L^2} + \frac{1-3\sin^2\alpha}{L^3}\right] \\
H_{xy}(\omega) &= H_{yx}(\omega) = 0 \\
H_{xz}(\omega) &= H_{zx}(\omega) = -\frac{1}{4\pi}\sin\alpha\cos\alpha\left[\frac{k_h^2}{L} + \frac{3ik_h}{L^2} - \frac{3}{L^3}\right]e^{ik_hL} \\
H_{yy}(\omega) &= \frac{1}{4\pi}e^{ik_v\xi}\left[\frac{k_h^2}{\lambda\xi} + \frac{ik_h}{L^2\sin^2\alpha}\right] - \frac{1}{4\pi}e^{ik_hL}\left[\frac{ik_h}{L^2\sin^2\alpha} - \frac{ik_h}{L^2} + \frac{1}{L^3}\right] \\
H_{yz}(\omega) &= H_{zy}(\omega) = 0 \\
H_{zz}(\omega) &= \frac{1}{4\pi L}\left[\left(1-\cos^2\alpha\right)k_h^2 + \frac{(1-3\cos^2\alpha)ik_h}{L} + \frac{3\cos^2\alpha-1}{L^2}\right]e^{ik_hL}
\end{aligned}
\tag{B1}
$$

$$y'_{11} = \frac{\lambda_1}{\lambda_2}\frac{k_{h2}{}^2}{k_{h1}{}^2} + \frac{\mu_2}{\mu_1}\frac{\xi_{v2}}{\xi_{v1}}, \ y'_{12} = \frac{\lambda_1}{\lambda_2}\frac{k_{h2}{}^2}{k_{h1}{}^2} - \frac{\mu_2}{\mu_1}\frac{\xi_{v2}}{\xi_{v1}}$$

$$m'_1 = \frac{\beta_1}{\xi_{v1}}e^{\lambda_1\xi_{v1}z_0}, \ m'_2 = \frac{\beta_2}{\xi_{v2}}e^{-\lambda_2\xi_{v2}z_0}$$

And

$$S_2 = \frac{2m''_1 - x''_{12}m''_2}{x''_{11}} \tag{A5}$$

$$T_1 = \frac{-y''_{11}m''_2 - y''_{12}S_2}{2} \tag{A6}$$

where

$$x''_{11} = \frac{\xi_{h2}}{\xi_{h1}} + \frac{\mu_2}{\mu_1}, \ x''_{12} = \frac{\xi_{h2}}{\xi_{h1}} - \frac{\mu_2}{\mu_1}$$

$$y''_{11} = \frac{\xi_{h2}}{\xi_{h1}} + \frac{\mu_2}{\mu_1}, \ y''_{12} = \frac{\xi_{h2}}{\xi_{h1}} - \frac{\mu_2}{\mu_1}$$

$$m''_1 = \beta_1 e^{\xi_{h1}z_0}, \ m''_2 = \beta_2 e^{-\xi_{h2}z_0}$$

where the conductivity-anisotropy $\lambda^2 = \sigma_h/\sigma_v$, $k_h = i\omega\mu\sigma_h$ and $k_v = i\omega\mu\sigma_v$ after the displacement currents are neglected, $\xi = L\sqrt{\sin^2\alpha + \lambda^2\cos^2\alpha}$.

Then we use an inverse Laplace transform to calculate the time-domain magnetic field components. In transient applications, we measure the voltage $\mathbf{V}(t)$ at the receiver coil, which is proportional to the time derivate of the magnetic field according to Faraday's Law

$$\mathbf{V}(t) = -NS\mu\frac{\partial\mathbf{H}(t)}{\partial t} \tag{B2}$$

where N is the number of coils, S is the coil area.

Defining two functions

$$
\begin{aligned}
\theta_v &= \left(\frac{\mu\sigma_v}{4t}\right)^{1/2} \\
\theta_h &= \left(\frac{\mu\sigma_h}{4t}\right)^{1/2}
\end{aligned}
\tag{B3}
$$

And the voltage components in formation coordinate (x,y,z) system can be expressed as

$$V_{xx}(t) = NS\mu \left\{ \begin{array}{l} \dfrac{1}{4\pi^{3/2}t}\theta_h e^{-\theta_v^2\xi^2} \cdot \left(\dfrac{2\xi^2}{L^2\sin^2\alpha}\theta_v^2 - \dfrac{1}{L^2\sin^2\alpha} \right) - \dfrac{1}{4\pi^{3/2}t}\theta_h e^{-\theta_h^2 L^2} \\ \cdot \left[4L^2\left(1-\sin^2\alpha\right)\theta_h^4 + \dfrac{2}{\sin^2\alpha}\theta_h^2 - 4\theta_h^2 - \dfrac{1}{L^2\sin^2\alpha} \right] \end{array} \right\}$$

$$V_{xz}(t) = V_{zx}(t) = NS\mu \left(\dfrac{1}{4\pi^{3/2}t}\theta_h e^{-\theta_h^2 L^2} \cdot 4L^2\sin\alpha\cos\alpha\theta_h^4 \right)$$

$$V_{yy}(t) = NS\mu \left\{ \begin{array}{l} \dfrac{1}{4\pi^{3/2}t}\theta_v e^{-\theta_v^2\xi^2} \cdot \left(-4\xi^2\lambda\theta_v^4 + 6\lambda\theta_v^2 - \dfrac{2\xi^2}{L^2\sin^2\alpha}\theta_v\theta_h \right) + \dfrac{1}{4\pi^{3/2}t}\theta_h e^{-\theta_v^2\xi^2} \cdot \dfrac{1}{L^2\sin^2\alpha} \\ + \dfrac{1}{4\pi^{3/2}t}\theta_h e^{-\theta_h^2 L^2} \cdot \left(\dfrac{2}{\sin^2\alpha}\theta_h^2 - 2\theta_h^2 - \dfrac{1}{L^2\sin^2\alpha} \right) \end{array} \right\}$$

$$V_{zz}(t) = NS\mu \left\{ \dfrac{1}{4\pi^{3/2}t}\theta_h e^{-\theta_h^2 L^2} \cdot \left[4\theta_h^2 + 4L^2\left(\cos^2\alpha - 1\right)\theta_h^4 \right] \right\}$$

$$(B4)$$

Take $V_{zx}(t)$ and $V_{zz}(t)$ for example and expand the exponential functions by a polynomial series in the product $\theta_h^2 L^2$

$$e^{-\theta_h^2 L^2} = 1 - \theta_h^2 L^2 + \dfrac{\left(\theta_h^2 L^2\right)^2}{2} - \dfrac{\left(\theta_h^2 L^2\right)^3}{3!} + \dots \qquad (B5)$$

For large time t, the decay of cross component is proportional $t^{-7/2}$ and the coaxial component has the typical $t^{-5/2}$ decay. Other components can be analyzed in the same way.

After a rotation to the sonde coordinate (x',y',z') system, voltages measured at the receivers can be obtained.

References

Anderson, B., Chew, W.C., 1989. Transient response of some borehole mandrel tools. Geophysics 54 (2), 216−224. https://doi.org/10.1190/1.1442645.

Dutta, S.M., Reiderman, A., Schoonover, L.G., et al., 2012. New borehole transient electromagnetic system for reservoir monitoring. Petrophysics 53 (15), 222−232. https://doi.org/10.2118/146735-ms.

Gao, J., Zhao, A.B., Peng, F., et al., 2007. Inversion of array induction logs and its application. Petrol. Sci. 4 (3), 31−35. https://doi.org/10.1007/s12182-007-0005-x.

Guptasarma, D., Singh, B., 1997. New digital linear filters for Hankel J0 and J1 transforms. Geophys. Prospect. 45 (5), 745−762. https://doi.org/10.1046/j.1365-2478.1997.500292.x.

Hagiwara, T., 2011. Apparent dip and apparent anisotropy from multifrequency triaxial induction measurements. Geophysics 76 (1), F1−F13. https://doi.org/10.1190/1.3511349.

Hagiwara, T., 2012. Determination of dip and anisotropy from transient triaxial induction measurements. Geophysics 77 (4), D105−D112. https://doi.org/10.1190/geo2011-0503.1.

Hong, D.C., Xiao, J.Q., Zhang, G.Y., et al., 2013. Fast inverse the relative dip using cross-component in highly deviated well. Chin. J. Geophys. 56 (7), 2494−2501. https://doi.org/10.6038/cjg20130735 (in Chinese).

Hong, D.C., Xiao, J.Q., Zhang, G.Y., et al., 2014. Characteristics of the sum of cross-components of triaxial induction logging tool in layered anisotropic formation. IEEE Trans. Geosci. Rem. Sens. 52 (6), 3107−3115. https://doi.org/10.1109/tgrs.2013.2269714.

Itskovich, G.B., 2017. Downhole Transient Resistivity Measurements. U.S. Patent 2017/0242146 A1.

Johansen, H.K., Sorensen, K.I., 1978. Fast Hankel transforms. Geophys. Prospect. 27 (4), 876−901. https://doi.org/10.1111/j.1365-2478.1979.tb01005.x.

Lai, J., Wang, G.W., Wang, Z.Y., et al., 2018. A review on pore structure characterization in tight sandstones. Earth Sci. Rev. 177, 436−457. https://doi.org/10.1016/j.earscirev.2017.12.003.

Li, Q., Omeragic, D., Chou, L., et al., 2005. New directional electromagnetic tool for proactive geosteering and accurate formation evaluation while drilling. In: SPWLA 46th Annual Logging Symposium Extended Abstracts.

Li, H., Zhou, J., 2017. Distance of detection for LWD deep and ultra-deep azimuthal resistivity tools. In: SPWLA 58th Annual Logging Symposium Extended Abstracts.

Li, H., Wang, H., 2016. Investigation of eccentricity effects and depth of investigation of azimuthal resistivity LWD tools using 3D finite difference method. J. Petrol. Sci. Eng. 143, 211−225. https://doi.org/10.1016/j.petrol.2016.02.032.

Li, J.H., Farquharson, C.G., Hu, X.Y., 2016. Three effective inverse Laplace transform algorithms for computing time-domain electromagnetic responses. Geophysics 81 (2), E113−E128. https://doi.org/10.1190/geo2015-0174.1.

Li, K.S., Gao, J., Ju, X.D., et al., 2018. Study on ultra-deep azimuthal electromagnetic resistivity LWD tool by influence quantification on azimuthal depth of investigation and real signal. Pure Appl. Geophys. 175 (12), 4465−4482. https://doi.org/10.1007/s00024-018-1899-5.

Moran, J.H., Gianzero, S., 1979. Effects of formation anisotropy on resistivity-logging measurements. Geophysics 44 (7), 1266−1286. http://doi.org/10.1190/1.1441006.

Mogilatov, V.S., 2010. Electromagnetic logging in time domain with use of specific current pulses. U.S. Patent 9, 405, 034 B2.

Payton, C.D., Strack, K.M., Tabarovsky, L.A., 1999. Method and apparatus for measuring transient electromagnetic and electrical energy components propagated in an Earth formation. U.S. Patent 5 (955), 844.

Raiche, A.P., 1987. Transient electromagnetic field computations for polygonal loops on layered earths. Geophysics 52 (6), 785−793. https://doi.org/10.1190/1.1442345.

Shao, C.R., Zhang, F.M., Chen, G.X., et al., 2013. Study of real-time LWD data visual interpretation and geo-steering technology. Petrol. Sci. 10 (4), 477−485. https://doi.org/10.1007/s12182-013-0298-x.

Seydoux, J., Legendre, E., Mirto, E., et al., 2014. Full 3D deep directional resistivity measurements optimize well placement and provide reservoir-scale imaging while drilling. In: SPWLA 55th Annual Logging Symposium Extended Abstracts.

Sun, H.F., Li, X., Li, S.C., et al., 2013. Three-dimensional FDTD modeling of TEM excited by a loop source considering ramp time. Chin. J. Geophys. 56 (3), 1049−1064 (in Chinese). http://doi.org/10.6038/cjg20130333.

Swidinsky, A., Weiss, C.J., 2017. On coincident loop transient electromagnetic induction logging. Geophysics 82 (4), E211−E220. https://doi.org/10.1190/geo2017-0134.1.

Tabarovsky, L.A., Epov, M.I., Robinovich, M.B., 2001. Measuring formation anisotropy using multifrequency processing of transverse induction measurements. In: SPE Annual Technical Conference and Exhibition. https://doi.org/10.2118/71706-ms.

Tan, M.J., Gao, J., Zou, Y.L., et al., 2012. Environment correction method of dual laterolog in directional well. Chin. J. Geophys. 55 (4), 1422−1432 (in Chinese). :

Wang, H.J., 2004. Digital filter algorithm of the sine and cosine transform. Chin. J. Eng. Geophys. 1 (4), 329−335 (in Chinese). http://doi.org/10.3969/j.issn.1672-7940.2004.04.008.

Wang, L., Li, H., Fan, Y.R., 2019a. Bayesian inversion of logging-while-drilling extra-deep directional resistivity measurements using parallel tempering Markov chain Monte Carlo sampling. IEEE Trans. Geosci. Rem. Sens. 57 (10), 8026−8036. https://doi.org/10.1109/tgrs.2019.2917839.

Wang, L., Deng, S.G., Zhang, P., et al., 2019b. Detection performance and inversion processing of logging-while-drilling extra-deep azimuthal resistivity measurements. Petrol. Sci. 16 (5), 1015−1027. https://doi.org/10.1007/s12182-019-00374-4.

Wu, Z.G., Deng, S.G., He, X.Q., et al., 2020. Numerical simulation and dimension reduction analysis of electromagnetic logging while drilling of horizontal wells in complex structures. Petrol. Sci. 17, 645−657. https://doi.org/10.1007/s12182-020-00444-y.

Zhong, L.L., Li, J., Bhardwaj, A., et al., 2008. Computation of triaxial induction logging tools in layered anisotropic dipping formations. IEEE Trans. Geosci. Rem. Sens. 46 (4), 1148−1163. https://doi.org/10.1109/tgrs.2008.915749.

Zhou, Q., Gregory, D., Chen, S.Y., et al., 2000. Investigation on electromagnetic measurement ahead of drill-bit. IGRASS 4, 1745−1747. https://doi.org/10.1109/igarss.2000.857332.